ACS Sustainable Chemistry & Engineering

Research Article

pubs.acs.org/journal/ascecg

Synthesis, Oxygen Permeation, and CO_2-Tolerance Properties of $Ce_{0.8}Gd_{0.2}O_{2-\delta}$−$Ba_{0.95}La_{0.05}Fe_{1-x}Nb_xO_{3-\delta}$ Dual-Phase Membranes

Hongwei Cheng,*[,†,‡] Naijun Zhang,[†] Xiaolu Xiong,[†] Xionggang Lu,*[,†,‡] Hongbin Zhao,[§] Shenggang Li,[∥] and Zhongfu Zhou[†,‡]

[†]School of Materials Science and Engineering, Shanghai University, Shanghai 200072, People's Republic of China

[‡]State Key Laboratory of Advanced Special Steel, Shanghai University, Shanghai 200072, People's Republic of China

[§]College of Sciences, Shanghai University, Shanghai 200444, People's Republic of China

[∥]Shanghai Advanced Research Institute, Chinese Academy of Sciences, 100 Haike Road, Shanghai 201210, People's Republic of China

ABSTRACT: A series of CO_2-tolerant dual-phase dense oxygen permeable membranes of stoichiometry $Ce_{0.8}Gd_{0.2}O_{2-\delta}$−$Ba_{0.95}La_{0.05}Fe_{1-x}Nb_xO_{3-\delta}$ (CG−$BLF_{1-x}N_x$, x = 0, 0.025, 0.05, 0.10, and 0.15) were designed and prepared by the sol−gel method. Their stability regarding phase composition and structure, oxygen permeability, and CO_2-tolerant property were investigated by X-ray diffraction (XRD), thermogravimetry and differential scanning calorimetry (TG-DSC), and temperature-programmed desorption of oxygen (O_2-TPD). Results of the materials characterization showed excellent chemical compatibility between CG and $BLF_{1-x}N_x$ without the formation of any impurity phase after sintering at 1200 °C in air. The oxygen-permeation experiments showed that with increasing niobium content, the oxygen permeability of the CG−$BLF_{1-x}N_x$ membranes decreased slightly, but the compositional and structural stability in CO_2 atmosphere improved significantly. The 60 wt % CG−40 wt % $BLF_{0.9}N_{0.1}$ membrane showed simultaneously good oxygen permeability and excellent CO_2 tolerance, and the oxygen-permeation flux reached 0.195 mL·cm^{-2}·min^{-1} in pure CO_2 atmosphere at 925 °C using a 1.0 mm thick membrane. This work demonstrates that CG−$BLF_{1-x}N_x$ dual-phase membranes have great application potential for separating oxygen from highly concentrated CO_2 atmosphere.

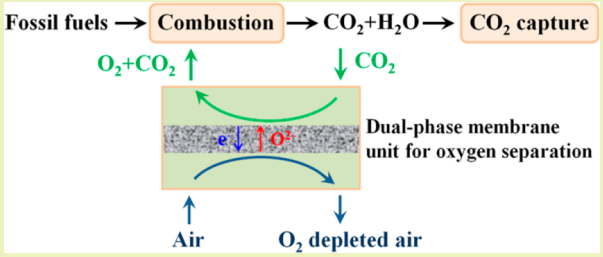

KEYWORDS: *Oxygen permeation, Dual-phase membrane, CO_2 tolerance, Stability*

INTRODUCTION

Recently, the reduction of carbon dioxide emission has become more and more important, and CO_2 capture, storage and utilization technologies have evolved into a research hotspot.[1,2] Oxygen-enriched combustion can result in a high concentration of CO_2, but it consumes a large amount of pure oxygen.[3] Dense mixed ionic−electronic conducting (MIEC) membranes have been attracting great attention because of their high selectivity toward oxygen (100%) at high temperatures (>700 °C), which can be used for producing oxygen from air, oxyfuel combustion for CO_2 capture, and partial oxidation of methane to syngas.[4,5] Compared with other membranes, perovskite-type oxygen-permeable membranes, such as $La_{1-x}Sr_xCo_{1-y}Fe_yO_{3-\delta}$[6] and $Ba_xSr_{1-x}Co_{0.8}Fe_{0.2}O_{3-\delta}$,[7] show high oxygen permeability, although their poor stability regarding phase composition and structure in CO_2 atmosphere limits their applications.[8,9]

To improve the CO_2-tolerance of these membranes, dual-phase oxygen-separation membranes were studied, which are composed of an oxygen ion-conducting phase and electron-conducting phase. In earlier research, noble metals were used as the electron-conducting phase. Chen et al.[10] studied a dual-phase membrane with the composition of noble metal Pd as the electron-conducting phase and yttria-stabilized cubic zirconia as the ion-conducting phase (YSZ−Pd). Wu et al.[11] prepared and examined $(Bi_2O_3)_{0.74}(SrO)_{0.26}$−Ag, which exhibited high electrical conductivity at room temperature. Kim et al.[12] investigated and compared the oxygen permeability of $Bi_{1.5}Y_{0.3}Sm_{0.2}O_3$ (BYS)−Ag and BYS−Au, and found that Ag doping could improve the oxygen exchange at the surface of the membrane. However, these kinds of membrane composed of an oxygen ionic conductor and a noble metal are unsuitable in practical applications because of their high cost, low mechanical strength, and poor oxygen permeability.[13] Perovskite-type (ABO_3) oxides have good oxygen permeability, high electronic conductivity combined with some ionic conductivity, which can replace noble metals as electron-conducting phases. Besides, oxides with the fluorite structure, such as $Ce_{0.9}Pr_{0.1}O_{2-\delta}$,[14] $Ce_{0.8}Sm_{0.2}O_{2-\delta}$,[15] and $Ce_{0.8}Gd_{0.2}O_{2-\delta}$,[16] exhibit good oxygen-ion conductivity, excellent phase stability in CO_2 atmosphere, and good chemical compatibility with perovskite-type oxides, which is beneficial for reducing the thermal expansion coefficients of dual-phase membranes. Therefore, they can significantly improve the CO_2-tolerance of dual-phase mem-

Received: March 10, 2015
Published: August 21, 2015

DOI: 10.1021/acssuschemeng.5b00693
ACS Sustainable Chem. Eng. 2015, 3, 1982−1992

branes if acting as oxygen ion-conducting phases. At present, much research on this kind of dual-phase oxygen-permeable membranes has been reported including $Ce_{0.8}Sm_{0.2}O_{2-\delta}$–$La_{0.8}Sr_{0.2}CrO_{3-\delta}$,[17] $Ce_{0.8}Sm_{0.2}O_{2-\delta}$–$PrBaCo_2O_{5+\delta}$,[18] and $Ce_{0.9}Gd_{0.1}O_{2-\delta}$–$Ba_{0.5}Sr_{0.5}Co_{0.8}Fe_{0.2}O_{3-\delta}$,[19] and all these materials showed good compositional and structural stability. In addition, research on other kinds of dual-phase membranes, such as perovskite–perovskite dual-phase membranes,[20] was also reported.

Numerous studies on perovskite-type oxygen-permeable membranes were carried out. Teraoka et al.[6] investigated $La_{0.6}A_{0.4}Co_{0.8}Fe_{0.2}O_{3-\delta}$ (A = Ba, Ga, Sr) and found that $La_{0.6}Ba_{0.4}Co_{0.8}Fe_{0.2}O_{3-\delta}$ exhibited the best oxygen permeability. Ishihara et al.[21] also found that partial or complete substitution of Ba at the A site could improve the oxygen permeability of perovskite-type oxides. There are some problems with cobalt-based perovskite-type oxides, such as high thermal expansion coefficients, poor stability, and high cost.[22] To overcome these problems, cobalt-free $BaFeO_{3-\delta}$-based perovskite-type oxides have been examined. Kida et al.[23] investigated a series of A-site substituted $BaFeO_{3-\delta}$-based membranes of stoichiometry $Ba_{0.95}M_{0.05}FeO_{3-\delta}$ (M = Na, Rb, Ca, Y, and La) and found that $Ba_{0.95}La_{0.05}FeO_{3-\delta}$ showed good phase stability and the highest oxygen permeability among the studied compounds. Watenabe et al.[24] prepared a 1.0 mm thick $Ba_{0.95}La_{0.05}FeO_{3-\delta}$ membrane, which exhibited a stable oxygen-permeation flux of 1.96 $mL{\cdot}cm^{-2}{\cdot}min^{-1}$ at 930 °C. However, there are few reports on using $Ba_{0.95}La_{0.05}FeO_{3-\delta}$ as the electron-conducting phase of dual-phase membranes.

In this work, $Ce_{0.8}Gd_{0.2}O_{2-\delta}$–$Ba_{0.95}La_{0.05}FeO_{3-\delta}$ dual-phase membranes have been prepared. The influence of the ratio of the two phases and the membrane thickness on the oxygen permeability was studied. To further improve the compositional and structural stability in CO_2 atmosphere, we doped the electronically conducting phase $Ba_{0.95}La_{0.05}FeO_{3-\delta}$ with niobium and prepared dense $Ce_{0.8}Gd_{0.2}O_{2-\delta}$–$Ba_{0.95}La_{0.05}Fe_{1-x}Nb_xO_{3-\delta}$ (x = 0, 0.025, 0.05, 0.10, and 0.15) dual-phase membranes. Doping of Nb inhibits the destruction of the lattice, and therefore enhances the thermal and structural stability of these membranes.[25] The oxygen permeability and the compositional and structural stability under CO_2 atmosphere of the membranes were systematically investigated.

EXPERIMENTAL SECTION

Materials Preparation. $Ba_{0.95}La_{0.05}Fe_{1-x}Nb_xO_{3-\delta}$ ($BLF_{1-x}N_x$ (x = 0, 0.025, 0.05, 0.10, and 0.15)) powders were synthesized by the sol–gel method.[26] According to the stoichiometry, the corresponding amounts of $Ba(NO_3)_2$, $La(NO_3)_3{\cdot}6H_2O$, $Fe(NO_3)_3{\cdot}9H_2O$, and niobium oxalate powders were weighed and dissolved in deionized water. Citric acid and EDTA were then added to form the sol with the molar ratio of total metal ions/EDTA/citric acid being 1:1:1.5. The pH was subsequently adjusted to 7–8 with ammonia. Drying at 85–95 °C was performed on a hot plate for gelation of the material. The gel was then calcined at 350 °C in air to remove organic residues. Finally, the powders were sintered at 850 °C for 8 h to obtain the $BLF_{1-x}N_x$ phase. Using a similar method, the $Ce_{0.8}Gd_{0.2}O_{2-\delta}$ (CG) powders were synthesized. The CG and $BLF_{1-x}N_x$ powders were mixed and ground with weight ratios of 4:6, 5:5, 6:4, and 7:3. The mixed powders were pressed to disks in a stainless steel mold at 140–150 MPa, and then these membranes were sintered at 1200 °C for 10 h to obtain finally the dense CG–$BLF_{1-x}N_x$ dual-phase membranes.

Materials Characterization. The phase composition and structure of the samples were characterized by X-ray diffraction (XRD, Rigaku D/MAX2550) using the Cu Kα radiation at the operation point of 40 kV and 200 mA.

The thermal characteristics of the samples were measured by thermogravimetry and differential scanning calorimetry (TG-DSC, NETZSCH STA 449 F3 Jupiter) at the heating rate of 10 K min^{-1} from 40 to 1100 °C in CO_2/N_2 atmosphere to investigate the CO_2 tolerance.

The oxygen desorption performance of the samples was measured by temperature-programmed desorption of oxygen (O_2-TPD, Micrometrics AutoChem II 2920). The samples were pretreated in pure He flow at 120 °C for 10 min in a U-type quartz tube and then cooled to 50 °C, followed by the oxygen-desorption process with the heating rate of 10 $K{\cdot}min^{-1}$ from 50 to 1050 °C in pure He carrier-gas flow.

The surface morphology of the fresh and used membranes was investigated by scanning electron microscopy (SEM, TESCAN FE-MIRA3-XM).

Oxygen-Permeation Measurements. The oxygen permeability of the CG–$BLF_{1-x}N_x$ dual-phase membranes was assessed in a self-made oxygen-permeation instrument, which was described in our previous work.[27] The sweep side of the membrane was sealed on a glass tube with a silver ring as the sealant, and the other side was jointed with a quartz tube representing the air side. He or CO_2 was fed to the sweep side at the flow rate of 100 $mL{\cdot}min^{-1}$ and dry air was fed to the air side of the membrane at the flow rate of 300 $mL{\cdot}min^{-1}$. The composition and concentration of the effluent gas was measured by an online gas chromatograph.

First-Principles Calculations. Density functional theory (DFT) calculations were carried out using the CASTEP program[28] in Materials Studio.[29] The exchange-correlation energy was calculated with the generalized gradient approximation (GGA) using the Perdew–Burke–Ernzerhof (PBE) functional.[30] Plane-wave basis sets based on ultrasoft pseudopotentials were used. The integration over the Brillouin zone was performed using the k-points generated with the Monkhorst–Pack scheme. Both $Ba_{19}LaFe_{20}O_{60}$ and $Ba_{19}LaFe_{18}Nb_2O_{60}$ are typical structures of ABO_3.[31] The space group is $Pm3m$. A supercell of 5 × 2 × 2 with a chemical formula of $Ba_{19}LaFe_{20}O_{60}$ was used in our modeling, and for a doping concentration of 2%, two Fe atoms were replaced by Nb atoms resulting in a chemical formula of $Ba_{19}LaFe_{18}Nb_2O_{60}$. All calculations were performed at 0 K. An energy cutoff of 300 eV and a k-point sample of 3 × 3 × 1 were used. Tolerances for the self-consistent calculations were set to 2×10^{-5} eV per atom for the total energy, 0.05 eV $Å^{-1}$ for the maximum force, 0.1 GPa for the maximum stress, and 0.002 Å for the maximum displacement. These parameters should give converged energy.[32] These DFT calculations were performed on the supercomputer at Shanghai Advanced Research Institute.

RESULTS AND DISCUSSION

Characterization of the Samples. Figure 1a shows the XRD patterns of the CG and partially B-site substituted $BLF_{1-x}N_x$ (x = 0, 0.025, 0.05, 0.10, and 0.15) powders, revealing single-phase materials. CG powder presents the pure fluorite structure, and $BLF_{1-x}N_x$ powders present the pure cubic perovskite structure, thereby indicating that Nb doping would not reduce the structural stability. With increasing Nb content, the main characteristic peaks of $BLF_{1-x}N_x$ move gradually toward lower angles because of the larger ionic radius of Nb^{5+} substituting the Fe sites, which leads to a lattice expansion.

Figure 1b presents the XRD patterns of the CG–BLF membranes with different weight ratios (CG:BLF = 4:6, 5:5, 6:4, and 7:3) after sintering at 1200 °C for 10 h in air. It is clearly evident that the characteristic peaks are composed of the fluorite phase (CG) and the perovskite phase (BLF), without any impurity phases being generated, indicating that there is no chemical reaction between CG and BLF and the chemical compatibility between the two phases is good. All investigated samples possess similar phase compositions, and the peak intensities of the fluorite phase and the perovskite phase reflect

DOI: 10.1021/acssuschemeng.5b00693
ACS Sustainable Chem. Eng. 2015, 3, 1982–1992

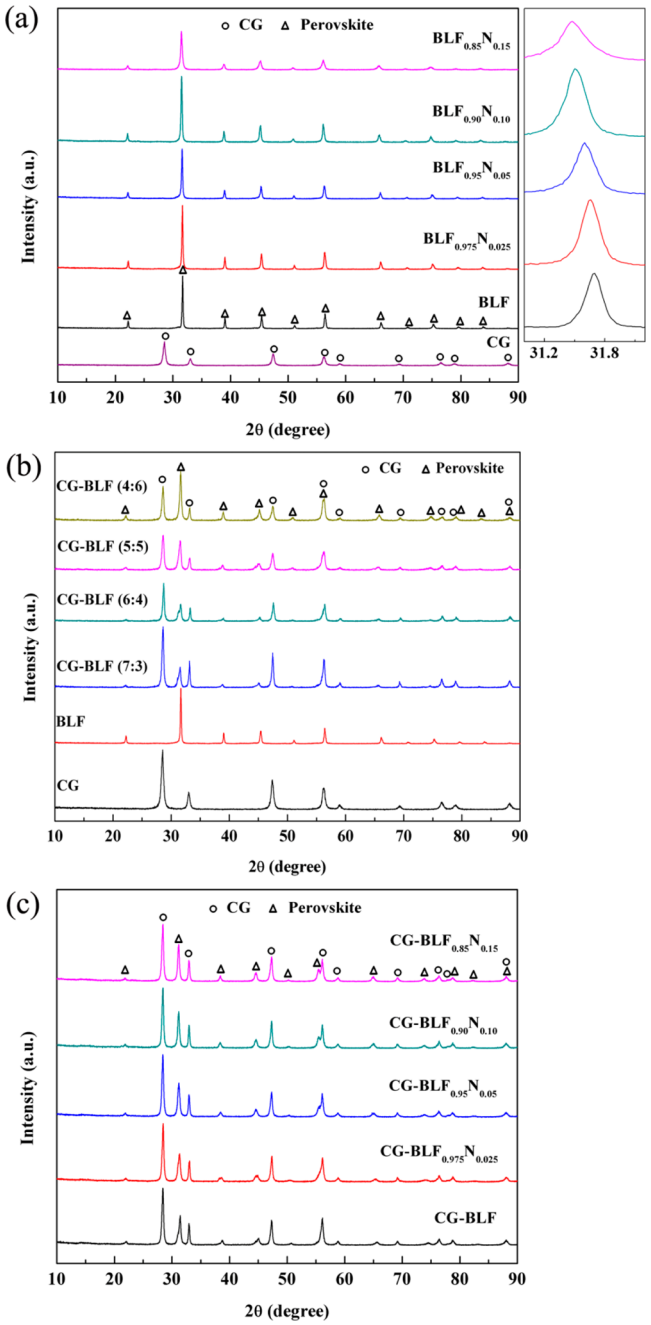

Figure 1. XRD patterns of the samples: (a) CG and $BLF_{1-x}N_x$ powders; (b) CG−BLF membranes of different compositions; (c) 60 wt % CG−40 wt % $BLF_{1-x}N_x$ membranes.

the content ratio of the two phases clearly. The XRD patterns of the dense 60 wt % CG−40 wt % $BLF_{1-x}N_x$ (x = 0, 0.025, 0.05, 0.10, and 0.15) dual-phase membranes are shown in Figure 1c. Again, the characteristic peaks are only composed of the fluorite phase (CG) and the perovskite phase ($BLF_{1-x}N_x$), which indicates that Nb doping has no negative effect on the chemical compatibility of the two phases.

Chemical Stability under CO_2-Containing Atmosphere. Figure 2 shows the O_2-TPD profiles of the CG, $BLF_{1-x}N_x$, and 60 wt % CG−40 wt % $BLF_{1-x}N_x$ (x = 0, 0.025, 0.05, 0.10, and 0.15) powders. The curves present that all $BLF_{1-x}N_x$ samples exhibit main desorption peaks between about 350 and 550 °C, because of O_2 release from the oxide

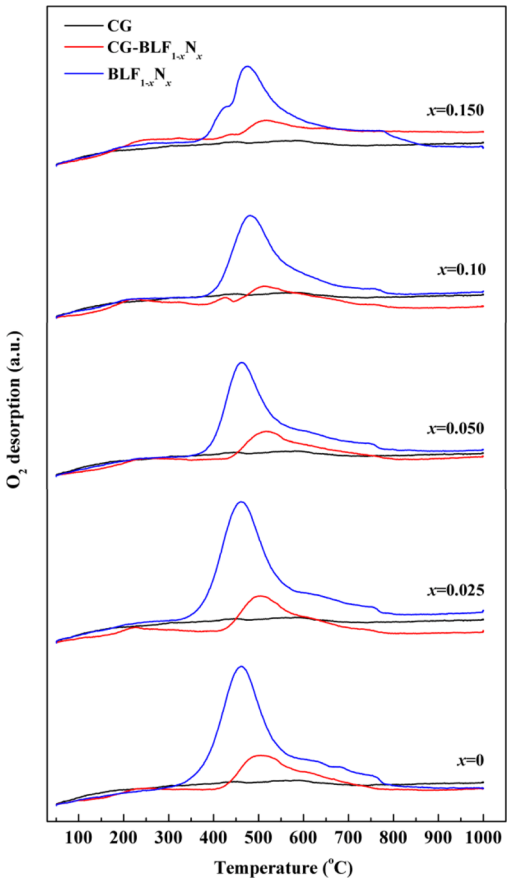

Figure 2. O_2-TPD profiles of CG, $BLF_{1-x}N_x$, and 60 wt % CG−40 wt % $BLF_{1-x}N_x$ powders.

lattice,[33,34] which corresponds to the reduction reaction of Nb^{5+}/Fe^{4+} to Nb^{4+}/Fe^{3+}.[35] The intensity of the main peak decreases gradually with increasing Nb content, indicating that the niobium dopant decreases the oxygen desorption properties of the perovskite phase. The CG curve does not exhibit an obvious desorption peak, thereby indicating that the fluorite oxide structure is very stable, which inhibits desorption of lattice oxygen.

The curve characteristics of the CG−$BLF_{1-x}N_x$ composite powders are approximate superpositions of the two single-phase curves with the area of the desorption peaks lying between those of the two individual phases CG and $BLF_{1-x}N_x$. However, compared to single-phase $BLF_{1-x}N_x$, the maximum peak of the CG−$BLF_{1-x}N_x$ curves moves toward higher temperatures This means that the occurrence of O_2 desorption needs higher temperatures, which indicates that the admixture of CG can restrain oxygen desorption and improves the chemical and thermal stability of the membranes.

Figure 3a,b shows the TG-DSC curves of single-phase CG and $BLF_{1-x}N_x$ (x = 0, 0.025, 0.05, 0.10, and 0.15) powders at the heating rate of 10 °C·min^{-1} from 40 to 1100 °C in 10 mol % O_2/N_2 and 20 mol % CO_2/N_2 atmosphere, respectively. Because of the desorption of lattice oxygen, all the $BLF_{1-x}N_x$ samples experience a weight loss above about 500 °C, which corresponds to the reduction reaction of Nb^{5+}/Fe^{4+} to Nb^{4+}/Fe^{3+},[35] similar to the result of O_2-TPD. In 20 mol % CO_2/N_2 atmosphere, with increasing temperature, the $BLF_{1-x}N_x$ samples experience different degrees of weight increase at about 850 °C and subsequent weight loss when the

DOI: 10.1021/acssuschemeng.5b00693
ACS Sustainable Chem. Eng. 2015, 3, 1982−1992

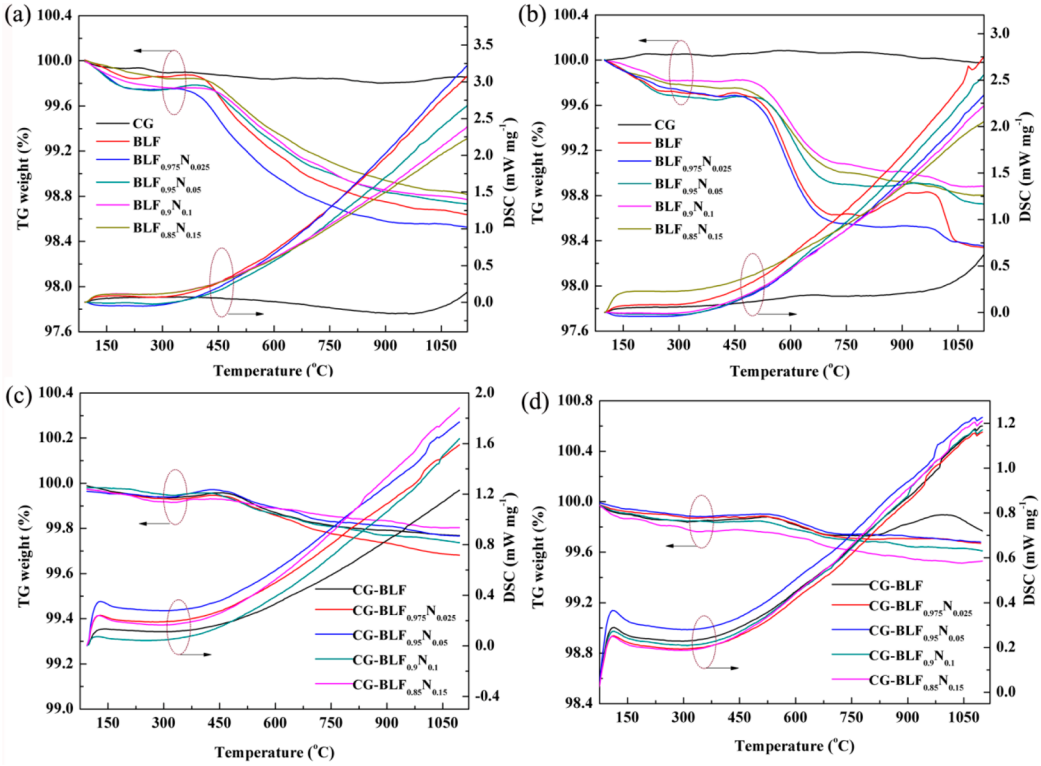

Figure 3. TG-DSC curves of the samples: (a) CG and $BLF_{1-x}N_x$ powders in 10 mol % O_2/N_2 atmosphere; (b) CG and $BLF_{1-x}N_x$ powders in 20 mol % CO_2/N_2 atmosphere; (c) 60 wt % CG−40 wt % $BLF_{1-x}N_x$ powders in 10 mol % O_2/N_2 atmosphere; (d) 60 wt % CG−40 wt % $BLF_{1-x}N_x$ powders in 80 mol % CO_2/N_2 atmosphere.

temperature reached about 1000 °C, which can be interpreted as such that the perovskite phases reacted with CO_2 to generate carbonates, and these carbonates decomposed at around 1000 °C.[25,36] The weight of BLF powder exhibits the most pronounced increase and shows an endothermic peak at 1080 °C in the DSC profile, indicating that the perovskite phase has transformed from an ordered to a disordered oxygen−vacancy phase.[37] On the other hand, the $BLF_{0.9}N_{0.1}$ and $BLF_{0.85}N_{0.15}$ powders have nearly no weight-increase peaks and the CG sample shows no obvious weight change at all.

Figure 3c,d presents the TG-DSC curves of the 60 wt % CGO−40 wt % $BLF_{1-x}N_x$ (x = 0, 0.025, 0.05, 0.10, and 0.15) dual-phase powders at the heating rate of 10 °C·min^{-1} from 40 to 1100 °C in 10 mol % O_2/N_2 and 80 mol % CO_2/N_2 atmosphere, respectively. The weight change trends of the dual-phase powders are similar to those of the $BLF_{1-x}N_x$ single-phase powders. It is worth noting that only CG−BLF in 80 mol % CO_2/N_2 atmosphere experiences a weight increase at about 850 °C and subsequent weight loss at about 1000 °C. Compared to the traditional perovskite-type membranes, the weight increment of composite CG−BLF is much smaller,[38] and even under the high CO_2 concentration of 80%, the Nb-doped membranes do not show weight-increase peaks. The primary result of these experiments implies that, compared to single perovskite materials, dual-phase membranes show stronger stability in CO_2 atmosphere and Nb doping can further improve the CO_2-tolerance of these dense dual-phase membranes.

To make a more accurate judgment on the CO_2-tolerance property of the CG−$BLF_{1-x}N_x$ (x = 0, 0.025, 0.05, 0.10, and 0.15) membranes, several groups of static experiments under CO_2 atmosphere have been done. Figure 4a shows the XRD patterns of 60 wt % CG−40 wt % $BLF_{0.9}N_{0.1}$ membranes after exposure to pure CO_2 atmosphere at temperatures in the range of 600−900 °C for 1 h. As evident, no impurity phase is generated in the samples at any temperature, which indicates that the CG−$BLF_{0.9}N_{0.1}$ membrane presents good thermal and chemical stability under CO_2 atmosphere. Meanwhile, extending the exposure time to 5, 10, 15, 20, and 40 h respectively, the CG−$BLF_{0.9}N_{0.1}$ membrane still keeps its original structure for up to 20 h, whereas the $BaCO_3$ impurity phase was generated after 40 h, as shown in Figure 4b, thereby reflecting the good CO_2 tolerance of the CG−$BLF_{0.9}N_{0.1}$ membrane. Figure 4c shows the XRD patterns of all 60 wt % CG−40 wt % $BLF_{1-x}N_x$ membranes after treatment in pure CO_2 atmosphere at 900 °C for 40 h. It can be seen that these CG−BLF samples generated obvious $BaCO_3$ impurity peaks. It is worth noting that the intensity of the reflections belonging to the ion-conducting phase CG with fluorite−oxide structure do not reveal any change, but that the reflections of the electron-conducting phase $BLF_{1-x}N_x$ with perovskite structure decrease obviously, because the perovskite-type oxide $BLF_{1-x}N_x$ reacts with CO_2 to form carbonates that destroy the perovskite crystal structure.[39] The fluorite oxide keeps its original peak intensity for the absence of any reaction. With increasing Nb content, the intensity of the $BaCO_3$ impurity peaks gradually decreased and that of the perovskite-phase peaks became less reduced, indicating that the CO_2 tolerance of the membranes can be strengthened by increasing the Nb content in CG−$BLF_{1-x}N_x$.

Oxygen-Permeation Performance. Different weight ratios of CG−BLF (4:6, 5:5, 6:4, and 7:3) membranes have been prepared to identify the best proportion between the oxygen ion-conducting and the electron-conducting phase. Figure 5a shows the oxygen-permeation fluxes of these samples

DOI: 10.1021/acssuschemeng.5b00693
ACS Sustainable Chem. Eng. 2015, 3, 1982−1992

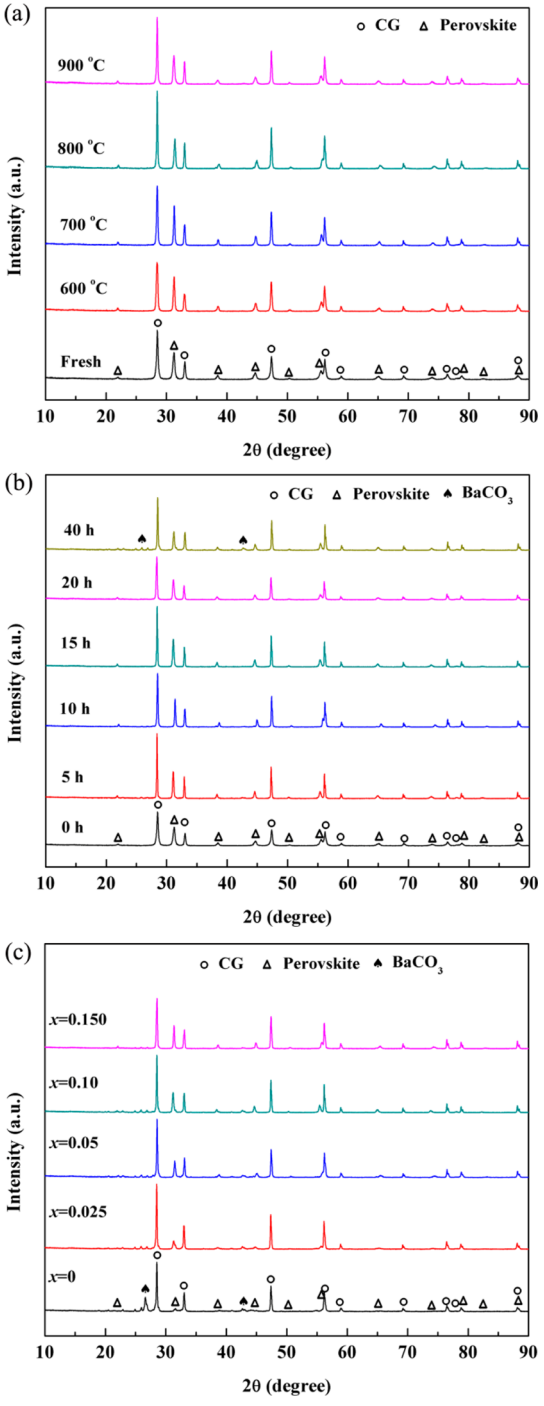

Figure 4. XRD patterns of 60 wt % CG−40 wt % $BLF_{0.9}N_{0.1}$ membranes after exposure to CO_2 atmosphere: (a) at different temperatures for 1 h; (b) for different times at 900 °C; (c) 60 wt % CG−40 wt % $BLF_{1-x}N_x$ membranes for 40 h.

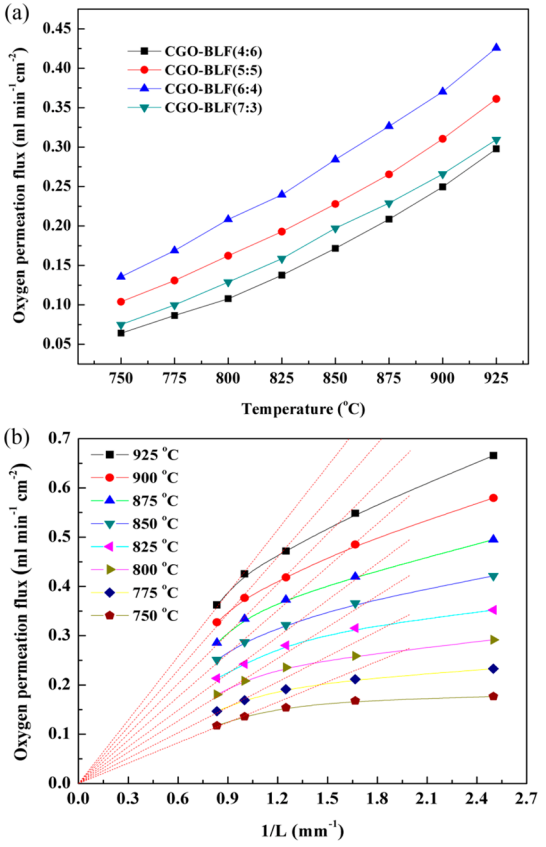

Figure 5. (a) Temperature dependence of the oxygen-permeation flux through 1.0 mm thick CG−BLF membranes of different composition; (b) temperature dependence of the oxygen-permeation flux through the 60 wt % CG−40 wt % BLF membrane for different thicknesses. Conditions: He flux of 100 $mL \cdot min^{-1}$ and air flux of 300 $mL \cdot min^{-1}$.

in dependence of temperature. It can be seen that the oxygen-permeation flux increases with temperature because of the temperature-enhanced bulk diffusion of oxygen ions and surface-exchange reactions.[40] The oxygen-permeation fluxes of these membranes in the sequence from high to low are as follows: 6:4 > 5:5 > 7:3 > 4:6. The oxygen-permeation flux of the 60 wt % CG−40 wt % BLF dual-phase membrane reaches 0.42 $mL \cdot cm^{-2} \cdot min^{-1}$ at 925 °C, being the highest oxygen-permeation flux among the investigated samples. The low oxygen permeability of the CG−BLF (4:6) membrane may be caused by a lack of the oxygen ion-conducting phase. With increasing CG content, a larger number of oxygen ion transport paths is formed, which enhances the oxygen-ion conductivity. However, when the CG content increases to 70 wt %, the oxygen-permeation flux begins to decrease because the excess of the oxygen ion-conducting phase cuts off connections of the electron-conducting phase, which leads to the reduction of the oxygen permeability. Consequently, if $CG_{wt\ \%}$:$BLF_{wt\ \%}$ = 6:4, the dual-phase membrane shows simultaneously good oxygen-ionic and electronic conductivity.

The oxygen-permeation process of dual-phase membranes includes two rate-determining steps, namely (a) the bulk diffusion rate of oxygen ions and electrons and (b) the surface exchange rate of oxygen. It can be concluded that if the bulk diffusion is the rate-determining step, decreasing the thickness is the easiest way to improve the oxygen permeability of the membranes.[41] To investigate the influence of the membrane thickness on the oxygen permeability and the attainable highest oxygen-permeation flux of this series of membranes when they are working normally, 60 wt % CG−40 wt % BLF membranes with the highest oxygen permeability were selected for further investigations. CG−BLF membranes were ground to thicknesses of 1.2, 1.0, 0.8, 0.6, and 0.4 mm and the oxygen-permeation fluxes of these samples in dependence of temperature are shown in Figure 5b. It can been seen that with decreasing thickness, the oxygen-permeation fluxes increase remarkably, indicating that in the thickness range of 0.4−1.2 mm, bulk diffusion is the rate-determining process of

DOI: 10.1021/acssuschemeng.5b00693
ACS Sustainable Chem. Eng. 2015, 3, 1982−1992

Table 1. Oxygen Permeation Fluxes of Various Dual-Phase Membranes Using CO_2/He as Sweep Gas

membrane type	temperature (°C)	thickness (mm)	J_{O_2} air/He (mL·cm^{-2}·min^{-1})	J_{O_2} air/CO_2 (mL·cm^{-2}·min^{-1})	ref
$Ce_{0.9}Pr_{0.1}O_{2-\delta}$–$Pr_{0.6}Sr_{0.4}FeO_{3-\delta}$	950	0.6	0.26	0.18	14
$Ce_{0.8}Sm_{0.2}O_{2-\delta}$–$La_{0.9}Sr_{0.1}FeO_{3-\delta}$	950	1.1	0.21	0.14	15
$Ce_{0.8}Sm_{0.2}O_{2-\delta}$–$La_{0.8}Sr_{0.2}CrO_{3-\delta}$	950	0.3	0.19		17
$Ce_{0.8}Sm_{0.2}O_{2-\delta}$–$PrBaCo_2O_{5+\delta}$	940	1.0	0.51		18
$La_{0.15}Sr_{0.85}Ga_{0.3}Fe_{0.7}O_{3-\delta}$–$Ba_{0.5}Sr_{0.5}Fe_{0.2}Co_{0.8}O_{3-\delta}$	915	1.99	0.45		20
$Ce_{0.8}Sm_{0.2}O_{1.9}$–$Sm_{0.6}Ca_{0.4}CoO_3$	950	0.5		0.19	35
$Ce_{0.8}Sm_{0.2}O_{2-\delta}$-$LaBaCo_2O_{5+\delta}$	950	0.6	0.62		42
$Ce_{0.85}Sm_{0.15}O_{3-\delta}$–$Sm_{0.6}Sr_{0.4}FeO_{3-\delta}$	950	0.6	0.41		43
$Ce_{0.9}Gd_{0.1}O_{2-\delta}$– Fe_2O_3	1000	0.5	0.18	0.16	44
$Ce_{0.8}Gd_{0.2}O_{2-\delta}$–$Ba_{0.95}La_{0.05}FeO_{3-\delta}$	925	0.4	0.68		this work
$Ce_{0.8}Gd_{0.2}O_{2-\delta}$–$Ba_{0.95}La_{0.05}Fe_{0.9}Nb_{0.1}O_{3-\delta}$	925	1.0		0.20	this work

oxygen permeation. Reducing the thickness of the membranes shortens the transmission path across the bulk phase, which contributes to the improvement in the transmission efficiency of electrons and oxygen ions.

Even the CG–BLF membrane with thickness of 0.4 mm has sufficient strength to endure the pressure of the experimental equipment and reveals proper functioning at different temperatures, thus revealing that the fluorite phase CG and the perovskite phase BLF have good chemical compatibility. The hybrid of the two phases has formed a tight structure and shows high physical strength. The oxygen-permeation flux of the 0.4 mm thick CGO–BLF membrane reaches 0.68 mL·cm^{-2}·min^{-1} at 925 °C. Compared with other research results listed in Table 1, this is quite a high value among dual-phase membranes. It can be concluded that the combination of CG and BLF exhibits excellent oxygen permeability and good structural stability.

A series of oxygen-permeation experiments have been done to investigate the influence of Nb doping on the oxygen permeability of these dual-phase membranes. Figure 6a shows the oxygen-permeation fluxes of 1.0 mm thick 60 wt % CG–40 wt % $BLF_{1-x}N_x$ membranes using helium as sweep gas at temperatures in the range of 750–925 °C. It can be seen that the oxygen-permeation flux increases with temperature, but slightly decreases with increasing Nb content. Research has shown that doping with high-valence ions could break the electrical neutrality of the perovskite phase. To maintain charge balance, the valence of the ion at the B site would decrease and the oxygen-vacancy concentration would reduce too, which means that doping with high-valence niobium ions induces the low-valence state of the ferric ions. The simultaneous decrease of the oxygen-vacancy concentration of the membrane reduces the transport channels of lattice oxygen. Furthermore, the bond energy of Nb–O ($\Delta H_{f,\ Nb-O,\ 289\ K}$ = 753 kJ·mol^{-1}) is higher than that of Fe–O ($\Delta H_{f,\ Fe-O,\ 289\ K}$ = 409 kJ·mol^{-1}), so that Nb doping enhances the average M–O bond energy and, as a result, the transmission resistance of lattice oxygen increases.[45] On the basis of this scenario, Nb doping would decrease the oxygen permeability of the CG–$BLF_{1-x}N_x$ membranes slightly.

Figure 6b shows the corresponding Arrhenius plots of the oxygen-permeation flux through the 60 wt % CG–40 wt % $BLF_{1-x}N_x$ membranes. All samples show a single apparent activation energy E_a for oxygen permeation at temperatures in the range of 750–925 °C. Tong et al.[46] suggested that an invariable activation energy is the hallmark of operational stability of MIEC membranes. The E_a values calculated according to Figure 6b are 59.64 ± 0.74, 70.79 ± 0.92, 99.37 ± 0.65, 101.75 ± 1.15, and 100.13 ± 1.12 kJ·mol^{-1} for CG–BLF, CG–$BLF_{0.975}N_{0.025}$, CG–$BLF_{0.95}N_{0.05}$, CG–$BLF_{0.9}N_{0.1}$, and CG–$BLF_{0.85}N_{0.15}$, respectively. The smaller the activation energy, the easier oxygen permeation proceeds. Among the studied samples, CG–BLF exhibits the smallest activation energy for oxygen permeation in the investigated temperature range, which can explain the highest oxygen permeability of all the samples.

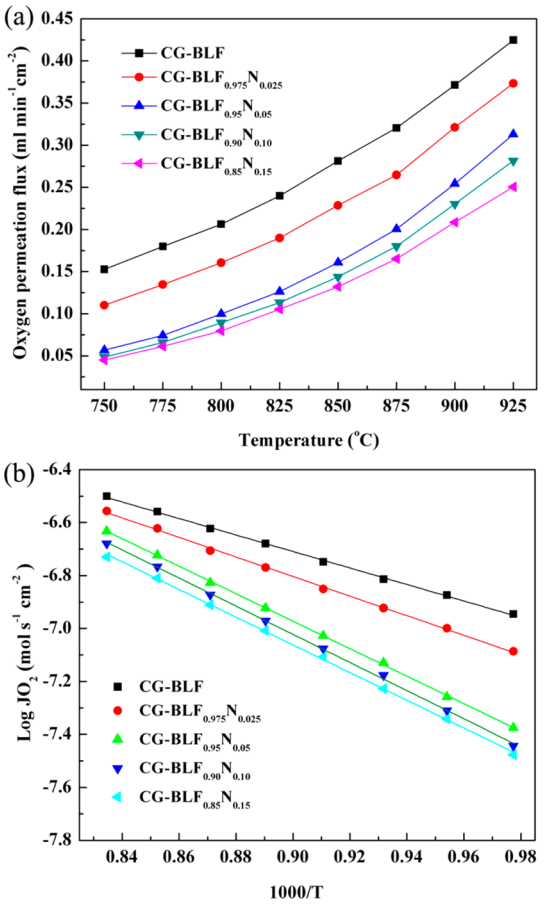

Figure 6. (a) Temperature dependence of the oxygen-permeation flux through 60 wt % CG–40 wt % $BLF_{1-x}N_x$ membranes and (b) corresponding Arrhenius plots. Conditions: He flux of 100 mL·min^{-1} and air flux of 300 mL·min^{-1}, thickness of 1.0 mm.

Optimized crystal structures of $Ba_{19}LaFe_{20}O_{60}$ and $Ba_{19}LaFe_{18}Nb_2O_{60}$ are shown in Figure 7, with their density of states shown in Figure 8a. Both $Ba_{19}LaFe_{20}O_{60}$ and $Ba_{19}LaFe_{18}Nb_2O_{60}$ are conductors,[47] and their energy bands

DOI: 10.1021/acssuschemeng.5b00693
ACS Sustainable Chem. Eng. 2015, 3, 1982–1992

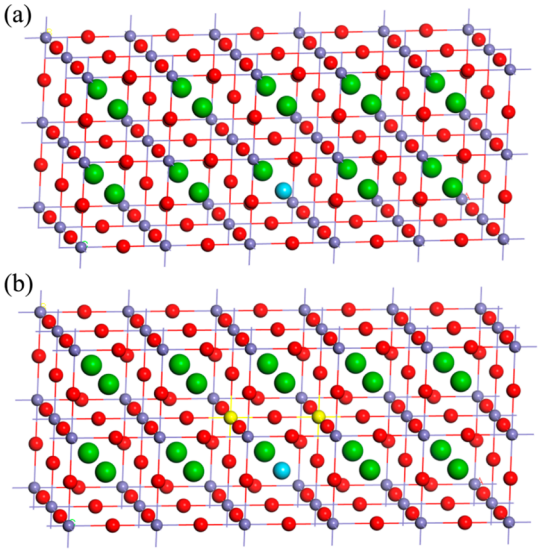

Figure 7. Structures of $Ba_{19}LaFe_{20}O_{60}$ and $Ba_{19}LaFe_{18}Nb_2O_{60}$; O in red, Ba in green, La in blue, Fe in purple, Nb in yellow.

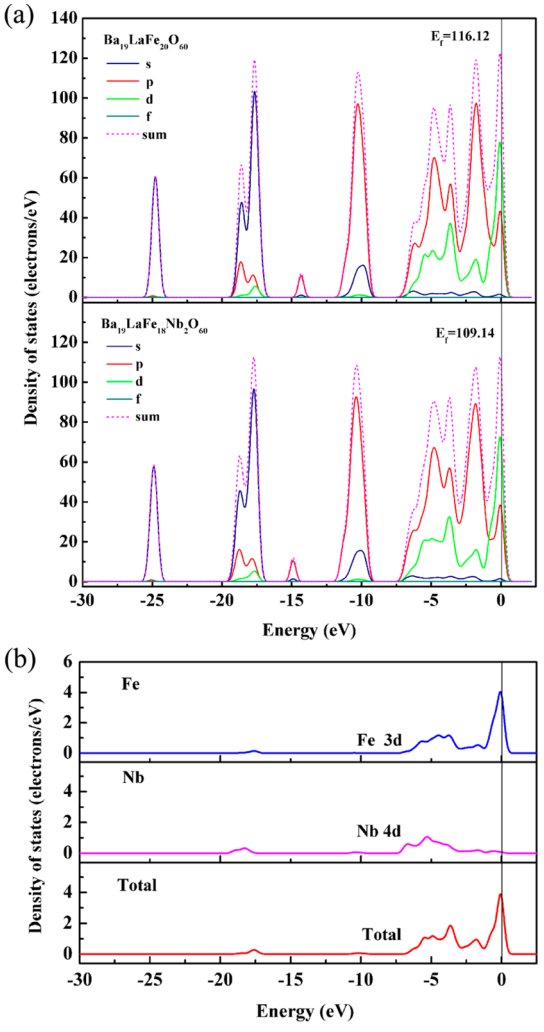

Figure 8. (a) Density of states for $Ba_{19}LaFe_{20}O_{60}$ and $Ba_{19}LaFe_{18}Nb_2O_{60}$; (b) density of states for atoms Fe and Nb in $Ba_{19}LaFe_{18}Nb_2O_{60}$.

can be divided into five parts from −25 to +1 eV.[48] The highest valence band is formed by the d orbits. The density of states at the Fermi level for $Ba_{19}LaFe_{20}O_{60}$ and $Ba_{19}LaFe_{18}Nb_2O_{60}$ are 116.12 and 109.14 eV respectively, indicating that the density of states decreases with the doping of Nb. For further analysis, at 0 K, the electrical conductivity can be expressed as follows:

$$\sigma = \frac{ne^2}{m_{e^*}}\tau(\varepsilon_F) \quad (1)$$

where n is the total electron density, ε_F is the half-filled band, τ is the relaxation time, σ is the electron conductivity, m_{e^*} is the average effective mass for the unoccupied states, e is the electron charge. Thus, the higher of the concentration of the quantum states, the higher the electrical conductivity. The permeation flux through the membrane is given by the Wagner equation below:[49]

$$J_{O_2} = -\frac{RT}{4^2F^2L}\int_{\ln P'_{O_2}}^{\ln P''_{O_2}} t_i t_e \sigma_{total} \mathrm{d}[\ln P_{O_2}] \quad (2)$$

In the above equation, R is the gas constant, T is the absolute temperature, F is Faraday's constant, L is the membrane thickness, and σ_{total} is the total electrical conductivity. Thus, the higher the value of σ_{total}, the higher the permeation flux. With the doping of Nb, the density of states at the Fermi level decreases, resulting in the decrease of the permeation flux, which is consistent with the experiment.

The density of states for the Fe and Nb atoms in the $Ba_{19}LaFe_{18}Nb_2O_{60}$ are shown in Figure 8b. At the Fermi level, the density of state for Fe is much higher than that of Nb, due to the much less concentration of Nb than Fe. With the further increase of the concentration of Nb, the density of states at the Fermi level will further decrease, resulting in even lower permeation flux.

Stability of Oxygen Permeation. Figure 9a shows the time dependence of oxygen-permeation fluxes through 60 wt % CG−40 wt % $BLF_{1-x}N_x$ membranes with different compositions of He and CO_2 of the sweep gases at 925 °C to investigate the oxygen permeability and chemical stability of these membranes in CO_2-containing atmosphere. The sweep gases of this experiment are switched in the following order: 100 mol % He, 15 mol % CO_2/He, 50 mol % CO_2/He, 100 mol % CO_2, and 100 mol % He and each atmosphere lasted for 10 h. Initially, when the sweep gas is 100 mol % He, the oxygen-permeation fluxes of the membranes are consistent with the results of the variable-temperature experiments shown in Figure 6a. With the proportion of CO_2 being increased, the oxygen-permeation fluxes of all the samples decrease because the perovskite phases form carbonates under CO_2 atmosphere at high temperature.[50] However, when the sweep gas is changed back to pure He, the oxygen-permeation fluxes almost recover to their initial values, which may be interpreted as indication that the CO_2-free sweep gas promotes carbonate decomposition and the recrystallization of the perovskite structure at high temperature. Only the oxygen-permeation fluxes of CG−BLF and CG−$BLF_{0.975}N_{0.025}$ present slight downward trends under 50 mol % of CO_2/He atmosphere. In the case the sweep gas is changed to 100 mol % of CO_2, the oxygen-permeation flux of CG−BLF decreases significantly, just slightly higher than that of CGO−$BLF_{0.85}N_{0.15}$ after 10 h. In the meantime, the oxygen-permeation fluxes of CG−$BLF_{0.95}N_{0.05}$, CG−$BLF_{0.9}N_{0.1}$, and CG−$BLF_{0.85}N_{0.15}$ have never decreased, indicating that the phase and structural stability of the membranes under CO_2

DOI: 10.1021/acssuschemeng.5b00693
ACS Sustainable Chem. Eng. 2015, 3, 1982−1992

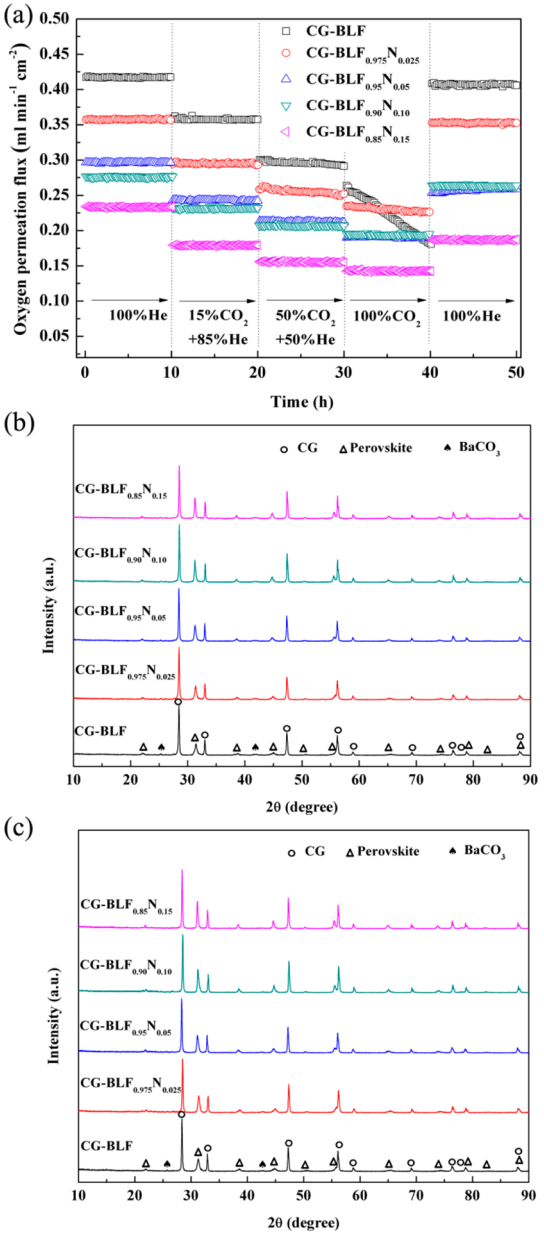

Figure 9. (a) Time dependence of the oxygen-permeation flux through CG−BLF$_{1-x}$N$_x$ membranes for different sweep gases; (b) XRD patterns of the air side after the experiments; (c) XRD patterns of the sweep side after the experiments. Conditions: T = 925 °C, air flux of 300 mL·min^{-1}, thickness of 1.0 mm.

atmosphere can be improved by increasing the Nb content. It should be noted that with increasing CO_2 concentration, the oxygen-permeation flux of CG−BLF$_{0.9}$N$_{0.1}$ decreases the least and is even higher than that of CG−BLF$_{0.95}$N$_{0.05}$ under 100 mol % CO_2 atmosphere, reaching 0.195 mL·cm^{-2}·min^{-1}, which is a very high value compared with the other research results listed in Table 1. In brief, the CG−BLF$_{0.9}$N$_{0.1}$ membrane shows the best oxygen permeability in pure CO_2 atmosphere of all investigated samples and simultaneously exhibits good CO_2 tolerance.

Figure 9b,c shows the XRD patterns of the air sides and sweep sides of the CG−BLF$_{1-x}$N$_x$ membranes after the permeation experiments, respectively. According to Figure 9b, only a few weak $BaCO_3$ impurity peaks can be observed at the air sides, because the majority of the carbonates has been decomposed under 100 mol % He atmosphere in the final stage of the experiment. A similar phenomenon is also found at the sweep sides presented in Figure 9c. With increasing Nb content in CG−BLF$_{1-x}$N$_x$, the $BaCO_3$ impurity peaks become gradually reduced, particularly at the sweep side of CG−BLF$_{0.85}$N$_{0.15}$ that even restores the original structure without any impurity phase. Consequently, compared with the pristine samples, the membranes after the permeation experiments can mainly keep the CG and BLF$_{1-x}$N$_x$ phases at both sides, thus confirming the good chemical stability of the CGO−BLF$_{1-x}$N$_x$ membranes.

To compare further the difference in CO_2 tolerance of the 60 wt % CG−40 wt % BLF and 60 wt % CG−40 wt % BLF$_{0.9}$N$_{0.1}$ membranes, we designed a long-time oxygen-permeation experiment for 100 h with pure CO_2 as sweep gas at 925 °C, as shown in Figure 10a. In the initial stage of this experiment,

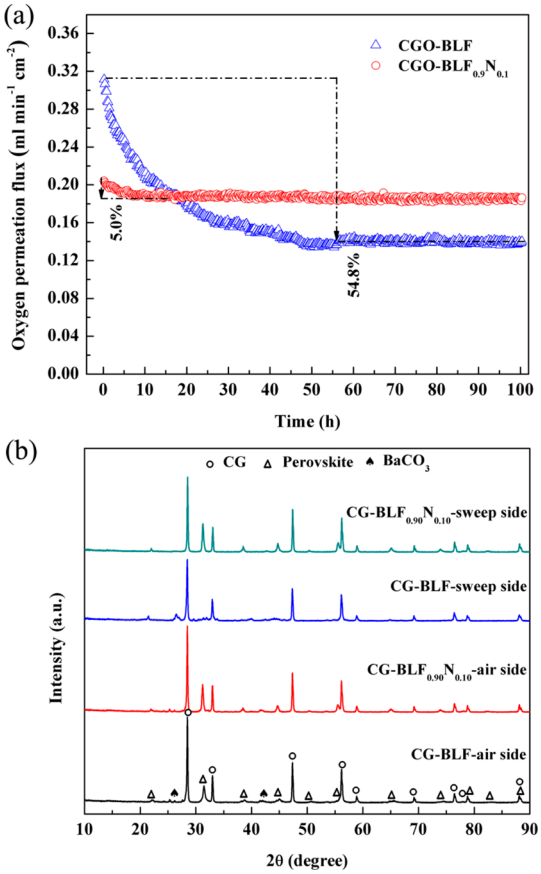

Figure 10. (a) Time dependence of the oxygen-permeation flux through the CG−BLF and CG−BLF$_{0.9}$N$_{0.1}$ membranes using pure CO_2 as sweep gas. Conditions: T = 925 °C, CO_2 flux of 100 mL·min^{-1}, air flux of 300 mL·min^{-1}, thickness of 1.0 mm. (b) XRD patterns of the CG−BLF and CG−BLF$_{0.9}$N$_{0.1}$ membranes after the experiments.

the oxygen-permeation flux of CG−BLF$_{0.9}$N$_{0.1}$ membrane is 0.20 mL·cm^{-2}·min^{-1}, lower than that of the CG−BLF membrane (0.31 mL·cm^{-2}·min^{-1}) because of the Nb doping. Because of the changed atmosphere, the oxygen-permeation fluxes of both membranes show downward trends at the early stage of the experiment. The oxygen-permeation flux of CG−BLF decreases significantly and becomes the lower one after about 15 h, whereas that of CG−BLF$_{0.9}$N$_{0.1}$ decreases only slightly. Finally, the oxygen-permeation flux of the CG−BLF

DOI: 10.1021/acssuschemeng.5b00693
ACS Sustainable Chem. Eng. 2015, 3, 1982−1992

membrane becomes stable after about 50 h, having decreased to 0.14 $mL \cdot cm^{-2} \cdot min^{-1}$ and the oxygen-permeation flux of the CG−$BLF_{0.9}N_{0.1}$ membrane becomes stable already after about 5 h, having decreased rather slightly to 0.19 $mL \cdot cm^{-2} \cdot min^{-1}$. Obviously, the Nb-doped CG−$BLF_{0.9}N_{0.1}$ membrane has a much better CO_2 tolerance.

The XRD patterns of the samples before and after the experiments are shown in Figure 10b. After working under CO_2 atmosphere for 100 h, both sides of the CG−BLF membrane are damaged obviously. The sweep side has generated $BaCO_3$ and the percentage of the perovskite phase decreased significantly, indicating that the BLF lattice is seriously damaged,[39] thus influencing the electronic conductivity of the membrane to some extent. By comparison, the compositional and structural stability of CG−$BLF_{0.9}N_{0.1}$ is much better: only a tiny amount of $BaCO_3$ impurities is generated at the surface, indicating a good long-term working stability under extreme operating conditions.

Figure 11 shows the morphology of the surface of the fresh as-sintered and the used dual-phase membranes of CG−BLF and CG−$BLF_{0.9}N_{0.1}$. From BSEM images of fresh membranes as shown in Figure 11b,d, it can be observed that ionic-conducting phase (the pale gray regions) and electronic-conducting phase (the dark gray regions) distribute relatively uniformly in the membranes with very small amounts of pinholes (the dark regions). Furthermore, a continuous distribution is found for both two phases. No obvious difference between the grain sizes of CG−BLF and CG−$BLF_{0.9}N_{0.1}$ indicates that the introduction of Nb has almost no effect on the grains sizes of the electronic-conducting or ionic-conducting phase. After operated under CO_2 atmosphere for 100 h, both air and sweep sides of CG−BLF and CG−$BLF_{0.9}N_{0.1}$ membranes are corroded in different extent, as presented in Figure 11e−h. The generant corrosion on the air side may result from the containing CO_2 in the feed compressed air.[19,51] In addition, it can be clearly seen that the corrosion on the sweep side of CG−BLF is more than that of CG−$BLF_{0.9}N_{0.1}$, which is consistent with the XRD result given in Figure 10b. Hence, the introduction of Nb in BLF can significantly lower its basicity and consequently enhance CO_2-tolerance of oxygen permeation membrane.

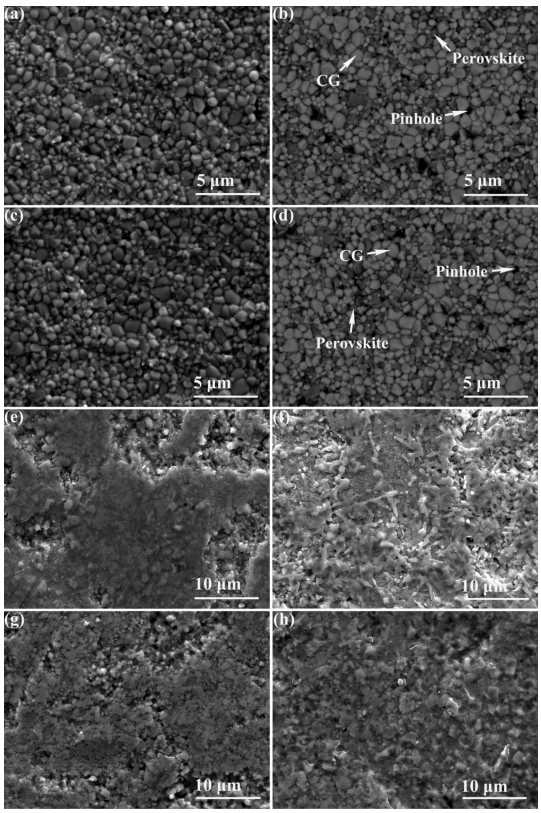

Figure 11. SEM images of the surfaces of the fresh (a) CG−BLF and (c) CG−$BLF_{0.9}N_{0.1}$, BSEM images of the surfaces of the fresh (b) CG−BLF and (d) CG−$BLF_{0.9}N_{0.1}$, SEM images of used membranes after the long-term experiment: the air side of (e) CG−BLF and (g) CG−$BLF_{0.9}N_{0.1}$; the permeation side of (f) CG−BLF and (h) CG−$BLF_{0.9}N_{0.1}$.

CONCLUSIONS

Dense $Ce_{0.8}Gd_{0.2}O_{2-\delta}$−$Ba_{0.95}La_{0.05}Fe_{1-x}Nb_xO_{3-\delta}$ (CG−$BLF_{1-x}N_x$, x = 0, 0.025, 0.05, 0.10, and 0.15) dual-phase membranes were synthesized by the sol−gel method for oxygen separation. The characterization results show that the chemical compatibility between the CG and $BLF_{1-x}N_x$ phases is good. Compared with the original CG−BLF membrane, Nb doping can improve the CO_2 tolerance and with increasing Nb concentration in CG−$BLF_{1-x}N_x$, the CO_2 tolerance is strengthened. The results of oxygen-permeation experiments show that the oxygen-permeation flux increases with temperature, but decreases slightly with the amount of Nb doping in CO_2-free atmosphere. The 60 wt % CG−40 wt % BLF membrane shows the highest oxygen permeability in He atmosphere at high temperature. However, in CO_2 atmosphere, the Nb-doped membranes clearly show better phase and structural stability. Among all investigated samples, the CG−$BLF_{0.9}N_{0.1}$ membrane exhibits the best oxygen permeability and simultaneously good CO_2-tolerance. The oxygen-permeation flux stabilizes at 0.19 $mL \cdot cm^{-2} \cdot min^{-1}$ for 100 h using pure CO_2 as sweep gas at 925 °C, which reveals that this dual-phase membrane has great application potential for separating oxygen from highly concentrated CO_2 atmospheres.

AUTHOR INFORMATION

Corresponding Authors

*Tel./Fax: +86-21-56335768. E-mail: hwcheng@shu.edu.cn (H. Cheng).

*Tel./Fax: +86-21-56335768. E-mail: luxg@shu.edu.cn (X. Lu).

Notes

The authors declare no competing financial interest.

ACKNOWLEDGMENTS

This work was supported by the National Natural Science Foundation of China (No. 51474145), the National Science Fund for Distinguished Young Scholars (No. 51225401), the Shanghai Rising−Star Program (15QA1402100) and Innovation Program of Shanghai Municipal Education Commission (No. 14YZ013).

REFERENCES

(1) Zhu, J. Y.; Baker, S. N. Lewis base polymers for modifying sorption and regeneration abilities of amine-based carbon dioxide capture materials. *ACS Sustainable Chem. Eng.* **2014**, *2*, 2666−2674.

(2) Wu, X. M.; He, G. H.; Yu, L.; Li, X. C. Electrochemical hydrogen pump with SPEEK/CrPSSA semi-interpenetrating polymer network proton exchange membrane for H_2/CO_2 separation. *ACS Sustainable Chem. Eng.* **2014**, *2*, 75−79.

DOI: 10.1021/acssuschemeng.5b00693
ACS Sustainable Chem. Eng. 2015, 3, 1982−1992

(3) Lin, H. Q.; Zhou, M. J.; Ly, J.; Vu, J.; Wijmans, J. G.; Merkel, T. C.; Jin, J. Y.; Haldeman, A.; Wagener, E. H.; Rue, D. Membrane-based oxygen-enriched combustion. *Ind. Eng. Chem. Res.* **2013**, *52*, 10820−10834.
(4) Sunarso, J.; Baumann, S.; Serra, J. M.; Meulenberg, W. A.; Liu, S. M.; Lin, Y. S.; Diniz da Costa, J. C. Mixed ionic−electronic conducting (MIEC) ceramic-based membranes for oxygen separation. *J. Membr. Sci.* **2008**, *320*, 13−41.
(5) Engels, S.; Markus, T.; Modigell, M.; Singheiser, L. Oxygen permeation and stability investigations on MIEC membrane materials under operating conditions for power plant processes. *J. Membr. Sci.* **2011**, *370*, 58−69.
(6) Teraoka, Y.; Zhang, H. M.; Furukawa, S.; Yamazoe, N. Oxygen permeation through perovskite-type oxides. *Chem. Lett.* **1985**, 1743−1746.
(7) Shao, Z. P.; Xiong, G. X.; Tong, J. H.; Dong, H.; Yang, W. S. Ba effect in doped $Sr(Co_{0.8}Fe_{0.2})O_{3-\delta}$ on the phase structure and oxygen permeation properties of the dense ceramic membranes. *Sep. Purif. Technol.* **2001**, *25*, 419−429.
(8) Schulz, M.; Kriegel, R.; Kämpfer, A. Assessment of CO_2 stability and oxygen flux of oxygen permeable membranes. *J. Membr. Sci.* **2011**, *378*, 10−17.
(9) Bochkov, D. M.; Kharton, V. V.; Kovalevsky, A. V.; Viskup, A. P.; Naumovich, E. N. Oxygen permeability of $La_2Cu(Co)O_{4+\delta}$ solid solutions. *Solid State Ionics* **1999**, *120*, 281−288.
(10) Chen, C. S.; Boukamp, B. A.; Bouwmeester, H. J. M.; Cao, G. Z.; Kruidhof, H.; Winnubst, A. J. A.; Burggraaf, A. J. Microstructural development, electrical properties and oxygen permeation of zirconia-palladium composites. *Solid State Ionics* **1995**, *76*, 23−28.
(11) Wu, K.; Xie, S.; Jiang, G. S.; Liu, W.; Chen, C. S. Oxygen permeation through $(Bi_2O_3)_{0.74}(SrO)_{0.26}$−Ag (40% v/o) composite. *J. Membr. Sci.* **2001**, *188*, 189−193.
(12) Kim, J.; Lin, Y. S. Synthesis and oxygen permeation properties of ceramic-metal dual-phase membranes. *J. Membr. Sci.* **2000**, *167*, 123−133.
(13) Zhu, X. F.; Li, Q. M.; Cong, Y.; Yang, W. S. Syngas generation in a membrane reactor with a highly stable ceramic composite membrane. *Catal. Commun.* **2008**, *10*, 309−312.
(14) Luo, H. X.; Jiang, H. Q.; Klande, T.; Cao, Z. W.; Liang, F. Y.; Wang, H. H.; Caro, J. R. Novel cobalt-free, noble metal-free oxygen-permeable $40Pr_{0.6}Sr_{0.4}FeO_{3-\delta}$- $60Ce_{0.9}Pr_{0.1}O_{2-\delta}$ dual-phase membrane. *Chem. Mater.* **2012**, *24*, 2148−2154.
(15) Wang, Z. T.; Sun, W. P.; Zhu, Z. W.; Liu, T.; Liu, W. A novel cobalt-free, CO_2-stable, and reduction-tolerant dual-phase oxygen-permeable membrane. *ACS Appl. Mater. Interfaces* **2013**, *5*, 11038−11043.
(16) Kharton, V. V.; Kovalevsky, A. V.; Viskup, A. P.; Figueiredo, F. M.; Yaremchenko, A. A.; Naumovich, E. N.; Marques, F. M. B. Oxygen permeability of $Ce_{0.8}Gd_{0.2}O_{2-\delta}$-$La_{0.7}Sr_{0.3}MnO_{3-\delta}$ composite membranes. *J. Electrochem. Soc.* **2000**, *147*, 2814−2821.
(17) Yi, J. X.; Zuo, Y. B.; Liu, W.; Winnubst, L.; Chen, C. S. Oxygen permeation through a $Ce_{0.8}Sm_{0.2}O_{2-\delta}$−$La_{0.8}Sr_{0.2}CrO_{3-\delta}$ dual-phase composite membrane. *J. Membr. Sci.* **2006**, *280*, 849−855.
(18) Chen, T.; Zhao, H. L.; Xie, Z. X.; Wang, J.; Lu, Y.; Xu, N. S. $Ce_{0.8}Sm_{0.2}O_{2-\delta}$- $PrBaCo_2O_{5+\delta}$ dual-phase membrane: Novel preparation and improved oxygen permeability. *J. Power Sources* **2013**, *223*, 289−292.
(19) Xue, J.; Liao, Q.; Wei, Y. Y.; Li, Z.; Wang, H. H. A CO_2-tolerance oxygen permeable $60Ce_{0.9}Gd_{0.1}O_{2-\delta}$−$40Ba_{0.5}Sr_{0.5}Co_{0.8}Fe_{0.2}O_{3-\delta}$ dual phase membrane. *J. Membr. Sci.* **2013**, *443*, 124−130.
(20) Wang, H. H.; Yang, W. S.; Cong, Y.; Zhu, X. F.; Lin, Y. S. Structure and oxygen permeability of a dual-phase membrane. *J. Membr. Sci.* **2003**, *224*, 107−115.
(21) Ishihara, T.; Fukui, S.; Nishiguchi, H.; Takita, Y. Mixed electronic-oxide ionic conductor of $BaCoO_3$ doped with La for cathode of intermediate-temperature-operating solid oxide fuel cell. *Solid State Ionics* **2002**, *152*, 609−613.
(22) Zhou, Q. J.; Zhang, L. L.; He, T. M. Cobalt-free cathode material $SrFe_{0.9}Nb_{0.1}O_{3-\delta}$ for intermediate-temperature solid oxide fuel cells. *Electrochem. Commun.* **2010**, *12*, 285−287.
(23) Kida, T.; Takauchi, D.; Watanabe, K.; Yuasa, M.; Shimanoe, K.; Teraoka, Y.; Yamazoe, N. Oxygen permeation properties of partially A-site substituted $BaFeO_{3-\delta}$ perovskites. *J. Electrochem. Soc.* **2009**, *156*, E187−E191.
(24) Watenabe, K.; Yuasa, M.; Kida, T.; Teraoka, Y.; Yamazoe, N.; Shimanoe, K. High-performance oxygen-permeable membranes with an asymmetric structure using $Ba_{0.95}La_{0.05}FeO_{3-\delta}$ perovskite-type oxide. *Adv. Mater.* **2010**, *22*, 2367−2370.
(25) Zhen, Q.; Yun, Q.; Wang, H. J.; Ding, C.; Ding, W. Z.; Lu, X. G. Investigation of chemical stability and oxygen permeability of perovskite-type $Ba_{0.5}Sr_{0.5}Co_{0.8}Fe_{0.2}O_{3-\delta}$ and $BaCo_{0.7}Fe_{0.2}Nb_{0.1}O_{3-\delta}$ ceramic membranes. *Solid State Ionics* **2011**, *189*, 50−55.
(26) Jiang, B.; Cheng, H. W.; Luo, L. F.; Lu, X. G.; Zhou, Z. F. Oxygen permeation and stability of $Ce_{0.8}Gd_{0.2}O_{2-\delta}$-$PrBaCo_{2-x}Fe_xO_{5+\delta}$ dual-phase composite membranes. *J. Mater. Sci. Technol.* **2014**, *30*, 1174−1180.
(27) Cheng, H. W.; Liu, J. Z.; Lu, X. G.; Ding, W. Z. Enhancing the oxygen permeability of $BaCo_{0.7}Fe_{0.2}Nb_{0.1}O_{3-\delta}$ membranes by coating $GdBaCo_{2-x}Fe_xO_{5+\delta}$ for partial oxidation of coke oven gas to syngas. *ACS Appl. Mater. Interfaces* **2011**, *3*, 4032−4039.
(28) Segall, M. D.; Lindan, P. J. D.; Probert, M. J.; Pickard, C. J.; Hasnip, P. J.; Clark, S. J.; Payne, M. C. First-principles simulation: ideas, illustrations and the CASTEP code. *J. Phys.: Condens. Matter* **2002**, *14*, 2717−2744.
(29) Accelrys Software Inc. *Materials Studio Release Notes*, Release 6.0; Accelrys Software Inc: San Diego, 2011.
(30) Perdew, J. P.; Burke, K.; Ernzerhof, M. Generalized Gradient Approximation Made Simple. *Phys. Rev. Lett.* **1996**, *77*, 3865−3868.
(31) Zhao, H. L.; Xu, N. S.; Cheng, Y. F.; Wei, W. J.; Chen, N.; Ding, W. Z.; Lu, X. G.; Li, F. S. Investigation of Mixed Conductor $BaCo_{0.7}Fe_{0.3-x}Y_xO_{3-\delta}$ with High Oxygen Permeability. *J. Phys. Chem. C* **2010**, *114*, 17975−17981.
(32) Zhang, X.; Fan, C.; Wang, Y.; Wang, Y.; Liang, Z.; Han, P. DFT +U predictions: The effect of oxygen vacancy on the structural, electronic and photocatalytic properties of Mn-doped BiOCl. *Comput. Mater. Sci.* **2013**, *71*, 135−145.
(33) Barbero, B. P.; Gamboa, J. A.; Cadús, L. E. Synthesis and characterisation of $La_{1-x}Ca_xFeO_3$ perovskite-type oxide catalysts for total oxidation of volatile organic compounds. *Appl. Catal., B* **2006**, *65*, 21−30.
(34) Sun, M.; Chen, X. W.; Hong, L. Influence of the interfacial phase on the structural integrity and oxygen permeability of a dual-phase membrane. *ACS Appl. Mater. Interfaces* **2013**, *5*, 9067−9074.
(35) Zhang, J.; Zhao, H. L.; Li, Y.; Xu, N. S.; Ding, W. Z.; Lu, X. G.; Li, F. S. Effects of iron content on the structural evolution, electrical properties and thermochemical stability of $BaCo_{0.9-x}Fe_xNb_{0.1}O_{3-\delta}$ ceramic membrane. *Int. J. Hydrogen Energy* **2010**, *35*, 814−820.
(36) Li, H. B.; Liu, Y.; Zhu, X. F.; Cong, Y.; Xu, S. P.; Xu, W. Q.; Yang, W. S. Oxygen permeation through Ca-contained dual-phase membranes for oxyfuel CO_2 capture. *Sep. Purif. Technol.* **2013**, *114*, 31−37.
(37) Babakhani, E. G.; Towfighi, J.; Shirazi, L.; Nakhaei Pour, A. Order-disorder transition and phase stability of $Ba_xSr_{1-x}Co_{0.8}Fe_{0.2}O_{3-\delta}$ oxides. *J. Membr. Sci.* **2011**, *376*, 78−82.
(38) Liu, J. Z.; Cheng, H. W.; Jiang, B.; Lu, X. G.; Ding, W. Z. Effects of tantalum content on the structure stability and oxygen permeability of $BaCo_{0.7}Fe_{0.3-x}Ta_xO_{3-\delta}$ ceramic membrane. *Int. J. Hydrogen Energy* **2013**, *38*, 11090−11096.
(39) Czuprat, O.; Arnold, M.; Schirrmeister, S.; Schiestel, T.; Caro, J. Influence of CO_2 on the oxygen permeation performance of perovskite-type $BaCo_xFe_yZr_zO_{3-\delta}$ hollow fiber membranes. *J. Membr. Sci.* **2010**, *364*, 132−137.
(40) Yacou, C.; Sunarso, J.; Lin, C. X.; Smart, S.; Liu, S. M.; Da Costa, J. C. D. Palladium surface modified $La_{0.6}Sr_{0.4}Co_{0.2}Fe_{0.8}O_{3-\delta}$ hollow fibres for oxygen separation. *J. Membr. Sci.* **2011**, *380*, 223−231.

DOI: 10.1021/acssuschemeng.5b00693
ACS Sustainable Chem. Eng. 2015, 3, 1982−1992

(41) Kobayashi, K.; Nishioka, M.; Sato, K.; Inoue, T.; Hamakawa, S.; Tsunoda, T. Synthesis and oxygen permeation properties of 75 mol% $Ce_{0.75}Nd_{0.25}O_{1.875}$-25 mol% $Nd_{1.8}Ce_{0.2}CuO_4$ composite. *J. Solid State Electrochem.* **2006**, *10*, 629−634.
(42) Chen, T.; Zhao, H. L.; Xu, N. S.; Li, Y.; Lu, X. G.; Ding, W. Z.; Li, F. S. Synthesis and oxygen permeation properties of a $Ce_{0.8}Sm_{0.2}O_{2-\delta}$-$LaBaCo_2O_{5+\delta}$ dual-phase composite membrane. *J. Membr. Sci.* **2011**, *370*, 158−165.
(43) Li, Q. M.; Zhu, X. F.; He, Y. E.; Cong, Y.; Yang, W. S. Effects of sintering temperature on properties of dual-phase oxygen permeable membranes. *J. Membr. Sci.* **2011**, *367*, 134−140.
(44) Luo, H. X.; Jiang, H. Q.; Efimov, K.; Liang, F. Y.; Wang, H. H.; Caro, J. R. CO_2-tolerant oxygen-permeable Fe_2O_3-$Ce_{0.9}Gd_{0.1}O_{2-\delta}$ dual phase membranes. *Ind. Eng. Chem. Res.* **2011**, *50*, 13508−13517.
(45) Sammells, A. F.; Cook, R. L.; White, J. H.; Osborne, J. J.; MacDuff, R. C. Rational selection of advanced solid electrolytes for intermediate temperature fuel cells. *Solid State Ionics* **1992**, *52*, 111−123.
(46) Tong, J. H.; Yang, W. S.; Zhu, B. C.; Cai, R. Investigation of ideal zirconium-doped perovskite-type ceramic membrane materials for oxygen separation. *J. Membr. Sci.* **2002**, *203*, 175−189.
(47) Lu, Y.; Zhao, H. L.; Cheng, X.; Jia, Y. B.; Du, X. F.; Fang, M. Y.; Du, Z. H.; Zheng, K.; Swierczek, K. Investigation of In-doped $BaFeO_{3-\delta}$ perovskite-type oxygen permeable membranes. *J. Mater. Chem. A* **2015**, *3*, 6202−6214.
(48) Islam, M. S. Computer modelling of defects and transport in perovskite oxides. *Solid State Ionics* **2002**, *154*−*155*, 75−85.
(49) Zhao, H. L.; Cheng, Y. F.; Xu, N. S.; Li, Y.; Li, F. S.; Ding, W. Z.; Lu, X. G. Oxygen permeability of A-site nonstoichiometric $Ba_xCo_{0.7}Fe_{0.2}Nb_{0.1}O_{3-\delta}$ perovskite oxides. *Solid State Ionics* **2010**, *181*, 354−358.
(50) Yi, J. X.; Schroeder, M.; Weirich, T.; Mayer, J. Behavior of $Ba(Co, Fe, Nb)O_{3-\delta}$ perovskite in CO_2-containing atmospheres: degradation mechanism and materials design. *Chem. Mater.* **2010**, *22*, 6246−6253.
(51) Luo, H. X.; Tian, B. B.; Wei, Y. Y.; Wang, H. H. Oxygen permeability and structural stability of a novel tantalum-doped perovskite $BaCo_{0.7}Fe_{0.2}Ta_{0.1}O_{3-\delta}$. *AIChE J.* **2010**, *56*, 604−610.

DOI: 10.1021/acssuschemeng.5b00693
ACS Sustainable Chem. Eng. 2015, 3, 1982−1992